

pubs.acs.org/cm Article

# New n-Type Zintl Phases for Thermoelectrics: Discovery, Structural Characterization, and Band Engineering of the Compounds $A_2CdP_2$ (A = Sr, Ba, Eu)

Adam Balvanz, Jiaxing Qu, Sviatoslav Baranets, Elif Ertekin, Prashun Gorai, and Svilen Bobev\*



Cite This: Chem. Mater. 2020, 32, 10697–10707



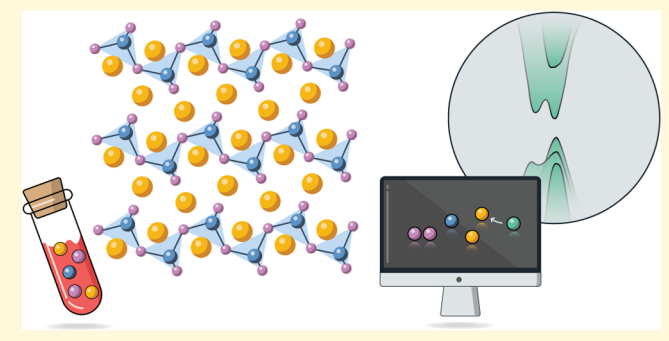
**ACCESS** 

III Metrics & More



S Supporting Information

ABSTRACT: Zintl phases, owing to their complex crystal structures and intricate chemical bonding, have recently been recognized as promising candidates for thermoelectric (TE) applications. Band engineering, including band convergence, has been shown to be an effective way to enhance the thermoelectric performance of such materials. In this work, a series of emerging TE materials, the isostructural Zintl phases with the general formula A<sub>2</sub>CdP<sub>2</sub> (A = Sr, Ba, Eu), are presented for the first time. Their structures, established from single-crystal X-ray diffraction methods, show them to crystallize with the orthorhombic Yb<sub>2</sub>CdSb<sub>2</sub> structure type, with first-principles calculations on phase stability confirming that Ba<sub>2</sub>CdP<sub>2</sub> and Sr<sub>2</sub>CdP<sub>2</sub> are



thermodynamically stable. Computationally, it was found that both Ba<sub>2</sub>CdP<sub>2</sub> and Sr<sub>2</sub>CdP<sub>2</sub> have the potential to exhibit high n-type TE performance (0.6 and 0.7 relative to the n-type PbTe, a reference TE material). To optimize the TE performance, band engineering strategies, including isovalent substitution and cation mutations, were investigated. From the band engineering of Ba<sub>2</sub>CdP<sub>2</sub> via isovalent substitution of Sr on a single Ba site, leading to the quaternary composition SrBaCdP<sub>2</sub>, it can be suggested that increasing the conduction band valley degeneracy is an effective way to improve the n-type TE performance by 3-fold. Moreover, first-principles defect calculations reveal that both Ba<sub>2</sub>CdP<sub>2</sub> and SrBaCdP<sub>2</sub> are n-type dopable, adding these compounds to a small list of rare n-type dopable Zintl phases. The band engineering strategies used in this work are equally applicable to other TE materials, either for optimization of existing TE materials or designing new materials with desired properties.

# 1. INTRODUCTION

The classification, known as the Zintl concept, was devised as a way to explain the complex bonding motifs present in certain types of intermetallic compounds. 1,2 This idea was originally developed by Zintl<sup>3</sup> and was later expanded upon by Klemm.<sup>4</sup> In most general terms, the Zintl-Klemm formalism considers the electropositive elements in the structure as donors of valence electrons, while the more electronegative elements are thought as electron acceptors. The latter atoms use the donated electrons to form covalent bonds, in a manner that the octet rules are satisfied for all constituents. As a result of this perceived electron-donation electron-acceptance scheme, the structures of many Zintl phases can be rationalized as having an anionic substructure (simple anions, or their formations in the form of clusters, chains, layers, or frameworks) and cations (spectator ions). Due to the complex bonding patterns, and the presence of both covalent and ionic bonding, Zintl phases have been widely explored for thermoelectric (TE) applications. For example, Yb<sub>14</sub>MnSb<sub>11</sub>,<sup>5</sup> Ca<sub>5</sub>Al<sub>2</sub>Sb<sub>6</sub>,<sup>6</sup> and Ba<sub>8</sub>Ga<sub>16</sub>Ge<sub>30</sub><sup>7</sup> are among the best performing TE materials and exhibit high TE figure of merit (zT > 1). The rationale behind this, as introduced above, is the complex crystal

structure of Zintl phases (layers, cages, channels, and other types of polyanionic moieties), which can lead to intrinsically low lattice thermal conductivity, while the presence of covalent bonding maintains moderately high carrier mobility. These characteristics fit within the "phonon-glass, electron-crystal" (PGEC)<sup>8</sup> concept, which is often used as a guiding principle in modern thermoelectric development.

As emphasized in the seminal reviews by Nesper<sup>1</sup> and Schäfer,<sup>9</sup> the chemistry of the Zintl phases, as well as intermetallic compounds in general, is an underdeveloped area of science. Three decades later, this is still true despite the growing interest in such compounds for TE and other applications. This vast and relatively uncharted phase-space allows for not only opportunities to discover new Zintl phases but also new TE materials with potentially high zT. To this

Received: October 8, 2020 Revised: November 20, 2020 Published: December 14, 2020





end, Zintl phases with a layered structure have garnered attention from the thermoelectric community: the "1-2-2" family (e.g., EuZn<sub>2</sub>Sb<sub>2</sub>), 10 "1-1-1" family (e.g., KSnSb), 11 and "2-1-2" family (e.g., Eu<sub>2</sub>ZnSb<sub>2</sub>), <sup>12</sup> to name just a few. The "1-2-2" family  $^{10,13,14}$  of layered Zintl phases crystallizing in the CaAl<sub>2</sub>Si<sub>2</sub> structure type, for example, exhibits low lattice thermal conductivities and high Seebeck coefficient, leading to highly competitive zT values (e.g., zT = 1.2 at 700 K for the system  $EuZn_{1.8}Cd_{0.2}Sb_2$ ). Solid solutions of Yb<sub>2-r</sub>Eu<sub>r</sub>CdSb<sub>2</sub>, <sup>15</sup> another new material with a layered structure, have shown moderate zT due to improved Seebeck coefficient in combination with the features inherited from the "parent" Yb<sub>2</sub>CdSb<sub>2</sub> structure. 16 The herein discussed newly synthesized phases, A<sub>2</sub>CdP<sub>2</sub> (A = Sr, Ba, Eu), also belong to the same layered structure type with space group Cmc21, and their thermoelectric assessment using computational methodology, specifically the quality factor  $\tilde{\beta}$ , 17 shows very promising n-type metrics. The TE performance of these phases can be further enhanced through modifying the electronic transport properties either by aliovalent doping, to control carrier concentrations, or by enhancing the Seebeck coefficient through band engineering. The focus of this work, though, will be the latter.

Band engineering of thermoelectric materials can be broadly classified into two categories: "resonant level" and "band convergence". Band structures can be engineered by modifying the relative energy of electronic bands to increase band degeneracy through alloying (band convergence), by introducing impurity energy levels that are resonant with the host band through resonant doping (resonant level), or a combination of both. Band convergence leads to multiple degenerate valleys in the band structure (Figure 1a), which can

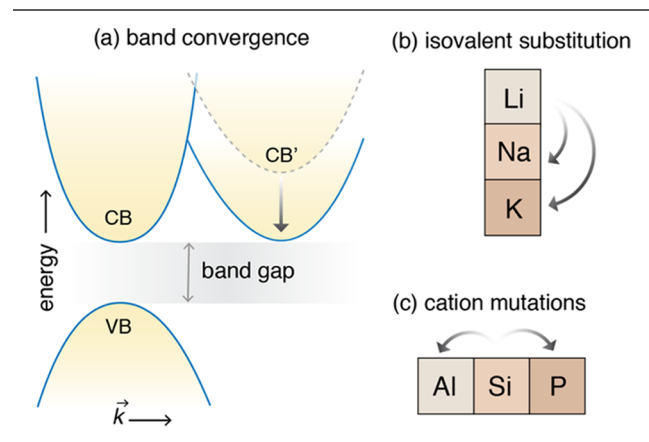


**Figure 1.** (a) Schematic of electronic band convergence. Here, the higher-energy conduction band (CB') is energetically converged with CB. Common strategies to induce band convergence include (b) isovalent substitution (substitute original atom with elements in same oxidation state) and (c) cation mutations (replace original cation with two or more cations while maintaining the same number of valence electrons).

simultaneously lead to high Seebeck coefficient and high electrical conductivity, provided the converging bands are dispersive, *i.e.*, low effective masses resulting in moderate to high carrier mobilities. This method has been successfully used to enhance power factors in well-known TE materials such as PbTe,  $^{20,23}$  Mg<sub>2</sub>Si,  $^{21}$  and Mg<sub>3</sub>Sb<sub>2</sub>. For example, Na doping in PbTe leads to valence band convergence of the light effective mass L band and heavy  $\Sigma$  band (0.2 eV away from L band

edge), allowing the PbTe system to achieve  $zT \approx 2.0$ , peaking at 800 K. <sup>25</sup> Beyond alloying, the possible strategies to induce band convergence include isovalent substitutions, wherein the original atom is substituted with elements in the same oxidation state (Figure 1b), and cation mutations, which involve replacing cations with two or more cations while simultaneously maintaining the same number of valence electrons (Figure 1c).

In this study, we explore combinations of both strategies to enhance the n-type TE performance of specifically Ba<sub>2</sub>CdP<sub>2</sub>. Based on the quality factor  $\beta_1^{17}$  the n-type TE performance of Ba<sub>2</sub>CdP<sub>2</sub> and Sr<sub>2</sub>CdP<sub>2</sub> is suggested to be moderate (0.6 and 0.7 relative to n-type PbTe, a reference TE material) and the TE performance can be enhanced by band engineering. Based on an analysis of the electronic band structures, we determined that band engineering via isovalent substitution of Sr on a single Ba site can improve the n-type TE performance of Ba<sub>2</sub>CdP<sub>2</sub> 3-fold through increasing the conduction band valley degeneracy. Moreover, first-principles defect calculations reveal that Ba2CdP2 and SrBaCdP2 are both n-type dopable, which is a rarity among Zintl phases. Ba<sub>2</sub>CdP<sub>2</sub> and SrBaCdP<sub>2</sub> reported in this work, therefore, add to the list of n-type dopable Zintl phases and will be important to study further to understand the doping asymmetry in Zintl phases.

# 2. EXPERIMENTAL AND COMPUTATIONAL METHODS

**2.1. Synthesis.** All synthetic and postsynthetic procedures were conducted either in an argon-filled glovebox or under vacuum. The elements used in the synthetic experiments (Ba, Cd, Eu, P, Pb, and Sr) were sourced from either Sigma-Aldrich or Alfa Aesar and had a stated purity of greater than 99 wt %. These elements were used as received. The starting materials were loaded into crucibles, which were subsequently flame-sealed in silica jackets. Once sealed, the vessels were placed into a programmable muffle furnace for heat treatment

All of the compounds presented here were synthesized using a Pb flux technique. Initially, both Eu<sub>2</sub>CdP<sub>2</sub> and Sr<sub>2</sub>CdP<sub>2</sub> were synthesized by loading the elements into alumina crucibles with a ratio designed to produce a set of compounds that were isostructural to the recently discovered Ba<sub>3</sub>Cd<sub>2</sub>P<sub>4</sub>. <sup>26</sup> As such, the elements were loaded with a 3:2:4:20 for Eu/Sr, Cd, P, and Pb, respectively (the Pb present was intended as flux, hence, the large stoichiometric excess). Ba<sub>2</sub>CdP<sub>2</sub>, on the other hand, was synthesized by loading the elements, in a 3.75:2:4:20 ratio (20-fold excess of Pb flux), into a custom-made crucible made from 0.375 in. (OD) niobium tubing. The highly reducing nature of the reaction mixture was shown to, in previous experiments, react at high temperatures with the standard alumina crucibles causing undesirable cracking. <sup>27,28</sup>

Single crystals of Eu<sub>2</sub>CdP<sub>2</sub> and Sr<sub>2</sub>CdP<sub>2</sub> were obtained by heating the reactants from 373 to 1173 K at a rate of 200 K/h. The peak temperature was held for 24 h and then slowly cooled to 823 K at a rate of 3 K/h. Once the temperature reached 823 K, the vessel was removed from the furnace and centrifuged at high speeds to separate the molten Pb flux from the grown crystallites. Ba<sub>2</sub>CdP<sub>2</sub> was synthesized in the same manner; however, during the cooling step of the reaction, a cooling rate of 2 K/h was used to promote the crystal growth of larger crystals.

Once the respective reactions were completed, the products were brought back in the argon-filled glovebox and prepared for further analysis. This step was necessary since freshly grown crystals of  $Ba_2CdP_2$  and  $Sr_2CdP_2$  showed visible signs of surface decomposition almost immediately after being exposed to the ambient atmosphere. The above is indicative of the air-sensitive materials, which ought to be handled with utmost care.

**2.2. Powder X-ray Diffraction (XRD).** The obtained samples were first examined by powder X-ray diffraction (XRD) at room

temperature. Powder XRD patterns were taken on a Rigaku MiniFlex powder diffractometer using filtered Cu K $\alpha$  radiation, which is operated inside a nitrogen-filled glovebox. A small portion of the obtained single crystals were ground inside an argon-filled glovebox using agate mortars and pestles. The data were collected between 5 and 70° in 2 $\theta$  with a step size of 0.05° and 2 s/step counting time. Once the crystal structures were elucidated based on single-crystal X-ray diffraction methods, the powder diffraction patterns were matched with the theoretically generated patterns, confirming the identity of the bulk.

**2.3. Single-Crystal X-ray Diffraction.** Data collections were made on single crystals from all of the compounds synthesized as a result of this inquiry. Crystals of suitable size were selected in an argon-filled glovebox and cut to size under an optical microscope in a drop of Paratone-N oil. The crystals were then picked up by a MiTeGen plastic loop and transferred to a Bruker APEX-II CCD diffractometer. A sealed X-ray source with Mo K $\alpha$  radiation ( $\lambda$  = 0.71073 Å) was employed. Temperature and inert atmosphere during the experiment were maintained by a system that uses 200 K nitrogen gas flow, obtained from boiling of liquid N<sub>2</sub>. The low temperature is needed to harden the Paratone-N oil, forming a shell around the crystal during the data acquisition.

Data were collected in batch runs covering nearly a hemisphere of the reciprocal space and were integrated and subsequently corrected for absorption using the Bruker-supplied software (SAINT and SADABS). The crystal structures were then solved using ShelXT, tutilizing  $O(ex2^{31})$  as a graphical interface. The structures were further refined using a full-matrix least-squares method on  $F^2$ , as implemented in the program SHELXL. Important crystallographic data from the three new structures are summarized in Table 1.

Table 1. Selected Crystallographic Data for  $A_2CdP_2$  (A = Sr, Ba, Eu)

empirical formula	$Ba_2CdP_2$	$Sr_2CdP_2$	$Eu_2CdP_2$			
formula weight (g/mol)	449.02	349.58	478.26			
temperature (K)		200(2)				
radiation		Mo K $\alpha$ , 0.71073 Å				
space group		$Cmc2_1$ (no. 36), $Z = 4$				
a (Å)	4.4730(6)	4.3256(18)	4.2975(4)			
b (Å)	17.015(2)	16.506(7)	16.3497(15)			
c (Å)	7.9244(11)	7.469(3)	7.3585(7)			
$V(Å^3)$	603.1(1)	533.2(4)	517.03(8)			
$ ho_{\rm cal}~({ m g/cm^3})$	4.95	4.35	6.11			
$\mu$ (cm <sup>-1</sup> )	167.8	243.0	284.7			
$R_1 (I > 2\sigma_{\rm I})^a$	0.0349	0.0392	0.0127			
$wR_2 (I > 2\sigma_I)^a$	0.0392	0.0459	0.0129			
$R_1$ (all data) <sup>a</sup>	0.0594	0.0664	0.0237			
$wR_2$ (all data) <sup>a</sup>	0.0606	0.0682	0.0237			
largest diff. peak/hole	1.53/-1.40	1.60/-1.10	0.71/-0.98			
${}^{a}R_{1} = \sum_{i=1}^{n}   F_{o}  -  F_{c}   / \sum_{i=1}^{n}  F_{o} ; wR_{2} = [\sum_{i=1}^{n} [w(F_{o}^{2} - F_{c}^{2})^{2}] / \sum_{i=1}^{n} [w(F_{o}^{2} - F_{o}^{2})^{2}] / \sum_{i=1}^{n} [w(F_{o}^{2} - F_{$						

A summary of the crystallographic work is given in Table 1. CCDC with the following reference numbers: 2034150 for Ba<sub>2</sub>CdP<sub>2</sub>; 2034151 for Sr<sub>2</sub>CdP<sub>2</sub>; and 2034152 for Eu<sub>2</sub>CdP<sub>2</sub> contain the full supporting crystallographic data for this paper. These files can be obtained free of charge via www.ccdc.cam.ac.uk/data\_request/cif or by contacting The Cambridge Crystallographic Data Centre, 12 Union Road, Cambridge CB2 1EZ, U.K.; fax: +44 1223 336033; email: data\_request@ccdc.cam.ac.uk.

 $(2F_c^2)/3$ ; A, B are the respective weight coefficients (please see CIF

files deposited at the CCDC as referenced in the text).

**2.4. Structure Relaxation and Electronic Band Structure.** Density functional theory (DFT) calculations were performed with Vienna Ab initio Simulation Package (VASP)<sup>33</sup> using projector

augmented wave (PAW) pseudopotentials. <sup>34</sup> For the exchange–correlation functional, we used the Perdew, Burke, and Ernzerhof (PBE) <sup>35</sup> version of the generalized gradient approximation (GGA). A plane-wave energy cutoff of 340 eV was used, which is found to give sufficiently converged total energies. The force and total energy convergence criteria used in this study were 0.01 eV/Å and  $10^{-6}$  eV, respectively. The electronic structures were calculated for the relaxed structures on a very dense k-point mesh of 8000/(number of atoms in cell), utilizing the tetrahedron method for performing k-point integrations. The band structures were calculated along the specific special k-point paths in the Brillouin zone. The high-symmetry k-points were determined using a methodology developed by Setyawan and Curtarolo. <sup>36</sup>

**2.5. Thermoelectric Performance Assessment.** The thermoelectric performance was computationally assessed with the quality factor  $^{17}$   $\beta$  defined as

$$\beta \propto \frac{\mu_0 m_{\rm DOS}^{*3/2}}{\kappa_{\rm L}} T^{5/2}$$
 (1)

where  $\mu_0$  is the intrinsic carrier mobility at 300 K,  $m_{DOS}^*$  is the density-of-states (DOS) effective mass,  $\kappa_L$  is the lattice thermal conductivity at 300 K, and T is the temperature. The quality factor  $^{17} \beta$ measures the maximal thermoelectric performance of materials under optimized carrier concentrations and can be directly evaluated from first-principles DFT calculations in a high-throughput fashion. It has been shown that  $\beta^{0.5}$  has a strong correlation with z corresponding to the peak zT across a diverse range of compounds. Therefore,  $\beta$  is predictive in assessing the maximal zT achievable when a material is optimally doped. Semiempirical models are developed for  $\kappa_L$  and  $\mu_{0}$ , which are based on ground-state DFT calculations (see previous works  $^{17,37}$  for details of the models).  $m_{\rm DOS}^*$  and band degeneracy  $N_{\rm b}$ are extracted from the electronic structures within a 150 meV energy window from the relevant band edges. Assuming identical and isotropic parabolic bands, the average band effective mass can be estimated by  $m_b^* = m_{DOS}^* N_b^{-2/3}$ . Bulk modulus (B) was obtained by fitting the Birch-Murnaghan equation of state to a set of total energies computed at different volumes (expansion and contraction around equilibrium volume).<sup>38</sup> For a more accurate estimate of the thermoelectric performance, one could employ higher levels of theory, e.g., DFT hybrid functionals, many-body GW methods, etc. Additionally,  $\kappa_L$  can be more accurately calculated by solving the Boltzmann transport equation<sup>39</sup> starting from the third-order anharmonic force constants (as implemented in Phono3py,<sup>40</sup> ShengBTE<sup>41</sup>) and molecular dynamics simulations.<sup>42</sup> Electronic transport parameters can be estimated by calculating the charge carrier scattering processes applied in well-known (e.g., EPW<sup>43</sup>) and emerging (e.g., AMSET, 44 Perturbo 45) software codes.

2.6. Stability Assessment. The thermodynamic stability of Ba<sub>2</sub>CdP<sub>2</sub> and Sr<sub>2</sub>CdP<sub>2</sub> against decomposition into competing phases was determined using the convex hull analysis. Binary and ternary competing phases from the Inorganic Crystal Structure Database<sup>4</sup> (ICSD) were considered in constructing the convex hull. We also considered the newly discovered Zintl phases Ba<sub>3</sub>Cd<sub>2</sub>P<sub>4</sub> and Ba<sub>2</sub>Cd<sub>2</sub>P<sub>3</sub> synthesized by Balvanz et al.<sup>26</sup> The total energies of the competing phases were calculated by relaxing the structure, using the same methodology as described before. The reference elemental chemical potentials were calibrated by fitting them to a set of experimental formation enthalpies, which has been shown to provide accurate predictions for formation enthalpies, 47 see the fitted reference elemental chemical potentials in the Supporting Information (Section S3). The phase stability region in chemical potential space is thermodynamically limited to several three-phase corners: at each corner, the "2-1-2" phase is in equilibrium with two other competing phases.

**2.7. Native Defect Chemistry.** To understand the native defect chemistry of the Zintl phases, we employed the standard supercell approach to calculate defect formation energies. The defect formation energy ( $\Delta E_{\mathrm{D},q}$ ) was calculated from the total energies as follows

$$\Delta E_{D,q} = E_{D,q} - E_{host} + \sum_{i} n_{i} \mu_{i} + q E_{F} + E_{corr}$$
 (2)

where  $\Delta E_{\mathrm{D},q}$  is the formation energy of a defect D in charge state q,  $E_{\mathrm{D},q}$  and  $E_{\mathrm{host}}$  are the total energies of the supercell with and without the defects, respectively,  $E_{\mathrm{F}}$  is the Fermi energy, which varies from the valence band maximum (VBM) to the conduction band minimum (CBM), and  $E_{\mathrm{corr}}$  is the term that accounts for the finite-size corrections within the supercell approach. The chemical potential of elemental species i is denoted by  $\mu_i$  and  $n_i$  is the number of atoms of species i added ( $n_i < 0$ ) or removed ( $n_i > 0$ ) from the host supercell to form defects.  $\mu_i$  is expressed as  $\mu_i = \mu_i^{\ 0} + \Delta \mu_i$ , where  $\mu_i^{\ 0}$  is the reference elemental chemical potential and  $\Delta \mu_i$  the deviation from the reference chemical potential. The bounds on  $\Delta \mu_i$  are set by the thermodynamic stability condition, with  $\Delta \mu_i = 0$  corresponding to i-rich conditions and a large negative value of  $\Delta \mu_i$  representing i-poor growth conditions.

For the defect calculations, we built supercells with 160 atoms and calculated the total energies by fully relaxing the atomic positions (keeping the volume and cell shape fixed). A plane-wave energy cutoff of 340 eV and Brillouin zone sampling using a 2  $\times$  2  $\times$  2 k-point grid were used to relax the supercells. The native point defects considered include vacancies ( $V_{Ba}$ ,  $V_{Sr}$ ,  $V_{Cd}$ ,  $V_{P}$ ) and antisite defects ( $Sr_{Ba}$ ,  $Ba_{Sr}$ ,  $Cd_{P}$ ,  $P_{Cd}$ ). The interstitial defects  $Ba_{i}$  are not considered in this work, given that the large ionic radius of Ba makes these defects energetically unfavorable. These native point defects are calculated in charged states ranging from -3 to +3. Furthermore, all unique Wyckoff positions in the structure (see in Table 2 and Figure 2) were considered for vacancies and antisite defects.

Table 2. Fractional Atomic Coordinates and Equivalent Displacement Parameters  $(U_{eq})^a$  for  $Ba_2CdP_2^b$ 

atom	x	у	z	$U_{ m eq}/{ m \AA}^2$	
Ba1	0	0.29615(6)	0.6105(1)	0.0136(2)	
Ba2	0	0.45930(6)	0.2754(1)	0.0128(2)	
Cd	0	0.09480(7)	0.4223(2)	0.0140(3)	
P1	0	0.0585(3)	0.0775(6)	0.0124(9)	
P2	0	0.3287(3)	0.0000(6)	0.012(1)	

 $^{a}U_{\rm eq}$  is defined as one-third of the trace of the orthogonalized  $U_{ij}$  tensor.  $^{b}$ The coordinates for the other two structures are tabulated in the Supporting Information (Table S1) and also available from the corresponding CIFs.

Among many approaches to compute finite-size corrections, we followed the approach proposed by Lany and Zunger<sup>48</sup> and included the following corrections to the defect formation energies: (1) image charge correction for charged defects, (2) potential alignment correction for charged defects, and (3) band-filling corrections for shallow defects. The static dielectric constant was calculated using the density functional perturbation theory (DFPT); the total static dielectric constant, which is the sum of the electronic and ionic contributions, enters the image charge correction. It is well known that GGA-PBE underestimates the band gap. To rectify this drawback of GGA-PBE, we also applied a band gap correction (through band edge shifts) based on state-of-the-art GW quasi-particle energy calculations. A computational framework for automating point defect calculations, pylada-defects, was utilized in this work for creating the defect supercells and analysis of the results, including calculation of the finite-size corrections.

# 3. RESULTS AND DISCUSSION

**3.1. Crystal Structure.** In this study, we report on the synthesis and structural characterization of three new ternary Zintl phases with layered structures, namely Ba<sub>2</sub>CdP<sub>2</sub>, Sr<sub>2</sub>CdP<sub>2</sub>, and Eu<sub>2</sub>CdP<sub>2</sub>. All three crystallize in a previously identified structure type: Yb<sub>2</sub>CdSb<sub>2</sub><sup>16</sup> in an orthorhombic base-centered crystal system with the space group *Cmc*2<sub>1</sub>. The structure is

noncentrosymmetric and has five independent atomic positions in the asymmetric unit (Table 2), including two unique Ba and P positions. Each atom in the structure is located at a Wyckoff 4a site having an m-symmetry.

The newly identified  $A_2CdP_2$  (A = Sr, Ba, Eu) compounds are members of a reasonably sized group of pnictides, inclusive of just one phosphide, Ca<sub>2</sub>CdP<sub>2</sub>, as well as several arsenides and antimonides—Ba<sub>2</sub>CdAs<sub>2</sub>, Eu<sub>2</sub>CdAs<sub>2</sub>, Sr<sub>2</sub>CdAs<sub>2</sub>, α-Ca<sub>2</sub>CdAs<sub>2</sub>, Ba<sub>2-x</sub>Yb<sub>x</sub>CdSb<sub>2</sub>, Sr<sub>2-x</sub>Ca<sub>x</sub>CdSb<sub>2</sub>, Sr<sub>2-x</sub>Yb<sub>x</sub>CdSb<sub>2</sub>,  $Ca_{2-x}Ba_xCdSb_2$ ,  $Sr_{2-x}Ba_xCdSb_2$ ,  $Eu_{2-x}Ba_xCdSb_2$ , and  $Yb_{2-x}Eu_xCdSb_2$ . Since the structural description of the prototype Yb<sub>2</sub>CdSb<sub>2</sub> is rather detailed, <sup>16</sup> our discussion here will be brief, and it will be concentrated on Ba<sub>2</sub>CdP<sub>2</sub>. One specific note is the increase in the unit cell volumes for A<sub>2</sub>CdP<sub>2</sub> in the order A = Eu, Sr, Ba (Table 1). There is an elongation (in all directions) of the lattice parameters, in that order. This can be easily explained by the trends seen in the ionic radii,<sup>53</sup> with Ba<sup>2+</sup> having the largest radius and Eu<sup>2+</sup> having the smallest one. One will notice the small margin: the Shannon ionic radius of  $\mathrm{Eu}^{2+}$  for coordination number 6 is 1.17 Å, while the corresponding ionic radius of Sr<sup>2+</sup> is 1.18 Å.<sup>53</sup> Despite the very small difference in their ionic radii, Eu<sub>2</sub>CdP<sub>2</sub> has a unit cell volume that is ca. 16 Å<sup>3</sup> (3%) reduced compared to that of Sr<sub>2</sub>CdP<sub>2</sub>. Similar unit cell parameter differences between Eucontaining compounds and their Sr-counterparts have been observed before. 54,55 In this regard, we should note that such dissimilarity might point to valence instabilities of Eu in Eu<sub>2</sub>CdP<sub>2</sub>, similar to that in Eu<sub>3</sub>InAs<sub>3</sub>, since Eu<sup>3+</sup> ions are smaller than Eu<sup>2+</sup>. However, at this time, there is no available experimental or computational data for Eu<sub>2</sub>CdP<sub>2</sub> to back this speculation.

The structure of Ba<sub>2</sub>CdP<sub>2</sub>, as seen projected down the crystallographic a-axis in Figure 2a, can be best described in the following manner. The Cd atoms present in the structure are coordinated to four P atoms in the form of slightly distorted tetrahedra (Figure 2b). This simple four-bonded fragment has three distinct bonds (ranging from 2.660(3) to 2.883(5) Å; tabulated distances for all three compounds can be found in the Supporting Information (Table S2)) attesting to the departure from the perfect  $T_d$  symmetry. We can also add that the shorter Cd-P distance is on par with the sum of the single-bonded radii of Cd and P, 1.5 and 1.1 Å, respectively. The bond angles also deviate somewhat from the ideal tetrahedral angle of 109.5°. Continuing, each individual tetrahedron shares all four of its vertices, P atoms, with another CdP<sub>4</sub> fragment. These linkages form a layer of cornershared tetrahedral, running parallel to the crystallographic a-cplane. These  $[CdP_2]^{4-}$  layers are stacked along the *b*-axis. Despite being called layers, they are not flat layers in the traditional sense, like those in graphite for instance: that is, the connections between the tetrahedra form a corrugated shape. Such an arrangement allows for all of the Ba atoms present in the structure to be in square pyramidal coordination to P atoms (Figure 2c,d). Using the Zintl-Klemm concept, the structure can be rationalized as [CdP<sub>2</sub>]<sup>4-</sup> polyanionic slabs (Figure 2b) and two divalent Ba<sup>2+</sup> cations needed to balance the charge. Therefore, the formula Ba2CdP2 is expected to correspond to a valence-precise compound, which should exhibit the characteristics of an intrinsic semiconductor. This notion is fully corroborated by the electronic structure calculations discussed in the following chapter.

Another relevant point of discussion concerns the "uniqueness" of the [CdP<sub>2</sub>]<sup>4-</sup> layers. By that, we mean the structural

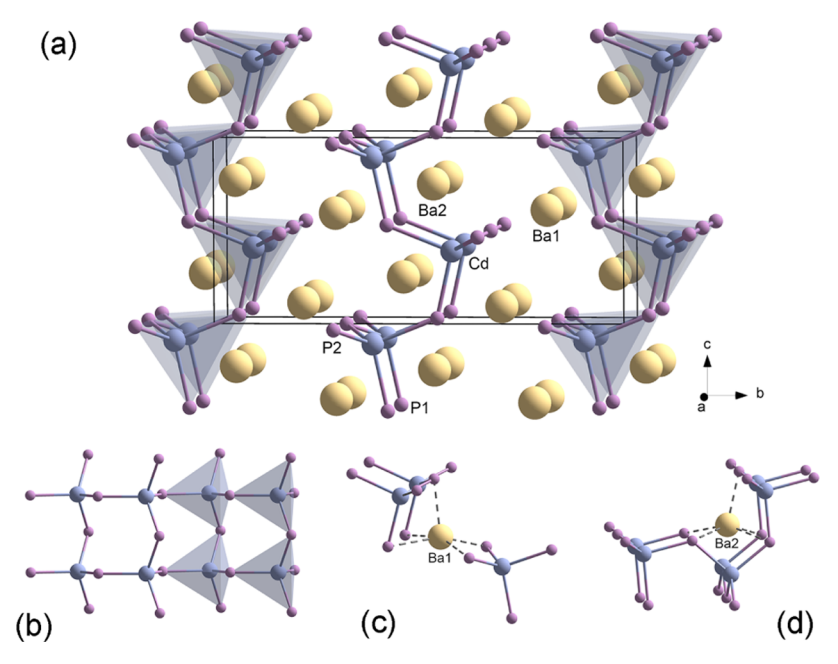


Figure 2. Schematic representation of the crystal structure of  $Ba_2CdP_2$ . (a) It represents the global structure as viewed down the crystallographic *a*-axis. The elements are represented as yellow, blue, and purple for Ba, Cd, and P, respectively. (b) It displays the polyanionic  $[CdP_2]^{4-}$  layers showing the corner-shared arrangement of the  $CdP_4$  tetrahedra. (c) It shows the coordination sphere of Ba1 (site 1) in the surrounding of two adjacent  $[CdP_2]^{4-}$  layers. (d) It depicts the coordination sphere of Ba2 (site 2) within a single  $[CdP_2]^{4-}$  layer.

comparison between Ba2CdP2 and the recently reported Ba<sub>2</sub>ZnP<sub>2</sub>. <sup>56</sup> The similarity of the chemical formulae is deceiving here, especially recognizing that Zn and Cd are both members of group 10 of the periodic table. The first of the "2-1-2" structures, as described already, is based on corner-shared CdP<sub>4</sub> tetrahedra forming [CdP<sub>2</sub>]<sup>4-</sup> layers. The second "2-1-2" structure contains a different [ZnP<sub>2</sub>]<sup>4-</sup> polyanionic fragment that consists of ZnP<sub>4</sub> tetrahedra forming infinite [ZnP<sub>2</sub>]<sup>4-</sup> chains. The ZnP<sub>4</sub> tetrahedra in Ba<sub>2</sub>ZnP<sub>2</sub> are edge-shared, whereas the CdP<sub>4</sub> tetrahedra in Ba<sub>2</sub>CdP<sub>2</sub> are corner-shared, forming layers. This difference in connectivity apparently does not originate from "electronic effects" as Zn and Cd are congeners; therefore, this structural difference must be attributed to "geometric effects" originated from the larger size of Cd. Additional discussion along these lines can be found in the computation part of this paper.

Last, we turn our attention to the Ba atoms present in Ba<sub>2</sub>CdP<sub>2</sub> both of which are located with distorted square pyramids of five neighboring P atoms. There are some subtle but important differences between the Ba1 and Ba2 positions. The Ba1 atoms present in the structure are located in between two layers (Figure 2c), and therefore, the coordination sphere "bridges" the two individual layers. The square plane, which is a part of the square pyramid, is comprised of two P2 atoms on one side and two P1 atoms on the other. These two different sides of the square plane are edges of CdP<sub>4</sub> tetrahedra, which are members of separate layers. This interlayer square plane is capped by a P2 atom that is a member of the layer containing the two P1 atoms mentioned previously. The bond distances within the coordination sphere of Ba1 vary from 3.136(5) to 3.345(4) Å. The distances are longer than the sum of the single-bonded radii of Ba and P, indicative of weak covalent character of the Ba-P interactions (unlike the Cd-P ones,

The coordination sphere of Ba2 is very similar to that of Ba1; however, the Ba2 atoms present in the structure are at the

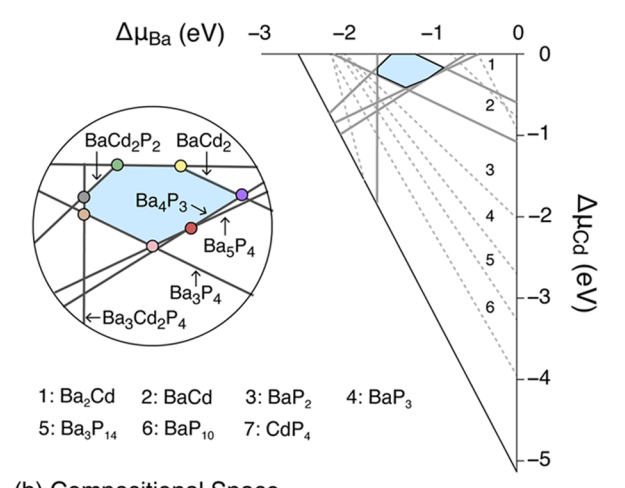
center of a distorted square pyramid geometry located within a single layer: that is to say, all five vertices (P atoms) are members of a single layer (Figure 2d). The base of the pyramid is comprised exclusively of P1 atoms, and the fifth vertex, capping the base, is a P2 atom. The distances Ba2–P1 and Ba2–P2 are comparable to those cited previously for the Ba1 coordination polyhedron and vary between 3.114(5) and 3.290(4) Å (Table S2).

It is important to note that the abovementioned square pyramidal coordination of Ba1 and Ba2 to P seems unusual for a large cation like  $Ba^{2+}$ ; however, such coordination spheres have been previously observed in  $Ca_{2-x}Ba_xCdSb_2$  and  $Sr_{2-x}Ba_xCdSb_2$ , as well as the structurally related  $K_2BaCdSb_2$ . Similarly, one of the  $Ba^{2+}$  cations in the structure of  $KBa_2Cd_2Sb_3$ , which is not layered, but rather three-dimensional (3D)-framework-like, is also found to exist in a square pyramidal coordination.

**3.2. Phase Stability.** Through convex hull construction, it was determined that Ba<sub>2</sub>CdP<sub>2</sub> and Sr<sub>2</sub>CdP<sub>2</sub> are thermodynamically stable phases. The calculated Ba–Cd–P ternary phase diagram is shown in both the chemical potentisal (Figure 3a) and composition space (Figure 3b). The computed Sr–Cd–P phase diagram can be found in the Supporting Information (Figure S2).

In the chemical potential space, the stability region of  $Ba_2CdP_2$  is restricted to a range of Ba, Cd, and P chemical potentials (shown by the light blue shaded region in Figure 3a). The phase stability region of  $Ba_2CdP_2$  is relatively large, indicating that it may be possible to tune the defect chemistry by regulating the growth conditions.  $\Delta\mu_{Ba}$ , which is the deviation from the elemental-phase reference potential, varies from -1.7 to -0.8 eV, suggesting  $Ba_2CdP_2$  is stable over a wide range of  $Ba_2$  chemical potentials. We also determined that P-rich growth condition is unattainable, with  $\Delta\mu_P$  varying from -1.4 to -0.9 eV.  $\Delta\mu_{Cd}$  varies over 0.4 eV, from -0.4 to 0.0 eV.  $Ba_2CdP_2$  can be, therefore, in equilibrium with elemental Cd

# (a) Chemical Potential Space



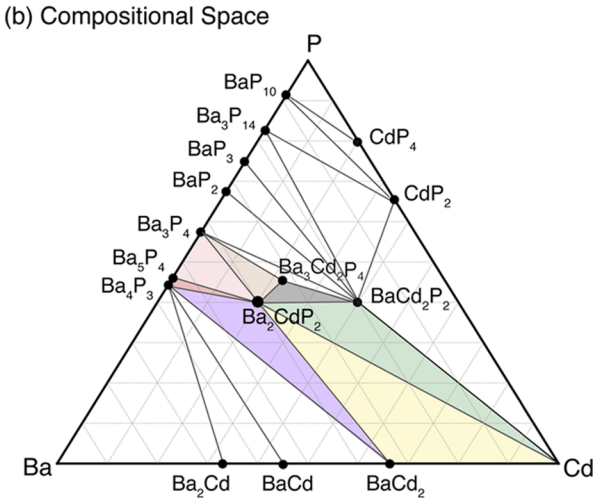


**Figure 3.** Phase stability region of  $Ba_2CdP_2$  in the (a) chemical potential space and (b) composition space. (a) Stability region of  $Ba_2CdP_2$  is shown by the shaded region. The competing phases are labeled. The circular inset is zoomed in on the stability region. (b) In composition space, the three-phase regions in equilibrium with  $Ba_2CdP_2$  are shaded.

under Cd-rich growth conditions ( $\Delta\mu_{Cd} = 0.0 \text{ eV}$ ), unlike Ba and P. We found that the phase stability region of Ba<sub>2</sub>CdP<sub>2</sub> is bounded by seven three-phase corners—at each corner, Ba<sub>2</sub>CdP<sub>2</sub> is in equilibrium with two other competing phases.

The competing phases that are in equilibrium with Ba<sub>2</sub>CdP<sub>2</sub> are BaCd<sub>2</sub>P<sub>2</sub> (trigonal, P3m1), BaCd<sub>2</sub> (orthorhombic, Imma), Ba<sub>4</sub>P<sub>3</sub> (orthorhombic, Pbam), Ba<sub>5</sub>P<sub>4</sub> (orthorhombic, Pnma), Ba<sub>3</sub>P<sub>4</sub> (orthorhombic, Fdd2), and Ba<sub>3</sub>Cd<sub>2</sub>P<sub>4</sub> (monoclinic, C2/m). At the most Ba-rich growth condition, Ba<sub>2</sub>CdP<sub>2</sub> is in equilibrium with BaCd<sub>2</sub> and Ba<sub>4</sub>P<sub>3</sub>. At the most Ba-poor chemical potential (gray and brown invariant point in Figure 3a and corresponding triangle region in Figure 3b), Ba<sub>2</sub>CdP<sub>2</sub> is in equilibrium with BaCd<sub>2</sub>P<sub>2</sub> and Ba<sub>3</sub>Cd<sub>2</sub>P<sub>4</sub>. BaCd<sub>2</sub>P<sub>2</sub> belongs to widely investigated AB<sub>2</sub>X<sub>2</sub>-type Zintl compounds (EuZn<sub>2</sub>Sb<sub>2</sub>, CaZn<sub>2</sub>Sb<sub>2</sub>, YbZn<sub>2</sub>Sb<sub>2</sub>, YbCd<sub>2</sub>Sb<sub>2</sub>, etc.), which adopts the CaAl<sub>2</sub>Si<sub>2</sub> structure, while Ba<sub>3</sub>Cd<sub>2</sub>P<sub>4</sub> was recently synthesized and is reported to be a rare n-type Zintl phase. 26 Sr<sub>2</sub>CdP<sub>2</sub> has a slightly "wider" phase stability region than Ba<sub>2</sub>CdP<sub>2</sub> in the chemical potential space (Figure S2 in the Supporting Information), which may lead to a larger singlephase region in the composition space. The phase stability

region for  $Sr_2CdP_2$  is bound by five three-phase corners. We found that  $Sr_2CdP_2$  is in equilibrium with the ternary phase  $SrCd_2P_2$  (trigonal,  $P\overline{3}m1$ ) and the binaries  $SrCd_{11}$  (tetragonal,  $I4_1/amd$ ),  $Sr_3P_4$  (orthorhombic, Fdd2), SrP (hexagonal,  $P\overline{6}2m$ ), and  $SrCd_2$  (orthorhombic, Imma).

This comprehensive phase stability analysis maps out the phase diagram more accurately, especially with the inclusion of the three newly discovered phases: Ba<sub>3</sub>Cd<sub>2</sub>P<sub>4</sub>, Ba<sub>2</sub>Cd<sub>2</sub>P<sub>3</sub>, <sup>26</sup> and Ba<sub>2</sub>CdP<sub>2</sub>. Also, it provides guidance for synthetic procedures, such as phase-boundary mapping, <sup>58</sup> wherein the growth condition of Ba<sub>2</sub>CdP<sub>2</sub> is controlled to pin the chemical potentials at one of the seven-phase stability corners (Figure 3a), achieving, for example, carrier control. Additionally, the range of chemical potentials in Figure 3a sets the range of  $\Delta\mu_i$  values in eq 1 for calculating the defect formation energies.

**3.3. Band Engineering of Ba<sub>2</sub>CdP<sub>2</sub>.** The thermoelectric performance of Ba<sub>2</sub>CdP<sub>2</sub> and Sr<sub>2</sub>CdP<sub>2</sub> were estimated with a quality factor  $\beta$ .<sup>17</sup> The following discussion is focused only on Ba<sub>2</sub>CdP<sub>2</sub> because it was found to be n-type dopable. At the outset, we must draw attention to the fact that this is an extremely rare case among Zintl phases (*vide infra*, Section 3.4).

The computed electronic and thermal transport properties, as well as the  $\beta$  values, are summarized in Table 3. The larger

Table 3. Computed Transport Properties and n-Type  $\beta^a$ 

phases	β	$eta/eta_{ ext{PbTe}}$	$m_b^*$	$N_{ m b,CB}$	$\frac{\kappa_{\rm L}}{({ m W/mK})}$	$(\text{cm}^2/(\text{Vs}))$
$Ba_2CdP_2$	8.9	0.59	0.119	1	1.8	105
$Sr_2CdP_2$	10.5	0.70	0.077	1	2.3	245
SrBaCdP <sub>2</sub>	24.4	1.62	0.067	2	2.0	278

<sup>a</sup>Here,  $m_b^*$  is band effective mass,  $N_{b,CB}$  is conduction band degeneracy,  $\mu_e$  is electron mobility, and  $\kappa_L$  is lattice thermal conductivity.  $\beta$  values are normalized by the n-type  $\beta$  of PbTe.

the value of  $\beta$ , the higher the predicted TE performance. Both "2–1–2" phases have moderately high  $\beta$  values (0.59 and 0.70 when compared to n-type PbTe), exhibiting low lattice thermal conductivities ( $\kappa_{\rm L} < 2.5~{\rm W/mK}$ ) and high electron mobilities ( $\mu_{\rm e} > 100~{\rm cm^2/(Vs)}$ ). However, the conduction band degeneracy for both compounds is only 1. The low conduction band degeneracy limits the thermopower, and therefore, the TE performance. It may be possible to increase the conduction band degeneracy via band engineering, thereby enhancing the n-type TE performance of Ba<sub>2</sub>CdP<sub>2</sub>.

Figure 4a presents the atom-decomposed electronic band structure of  $Ba_2CdP_2$ , showing that  $Ba_2CdP_2$  is a direct-gap semiconductor with a DFT-GGA computed band gap of 0.68 eV. The DFT calculation of electronic structure with GGA exchange—correlational functional, however, tends to underestimate the band gap; therefore, using state-of-the-art GW methods, we found that the band gap of  $Ba_2CdP_2$  is 1.43 eV.

The conduction band minimum (CBM) is singly degenerate and located at the  $\Gamma$  point, with a second conduction band valley located 0.25 eV above the CBM at the Z point (Figure 4a). We also calculated the electronic structure of  $Sr_2CdP_2$ , which is shown in Figure S3 of the Supporting Information. We find that the energy separation between the two conduction band valleys at  $\Gamma$  and Z is 0.35 eV. Convergence of this second valley with the one located at  $\Gamma$  offers the possibility of improving the n-type performance of  $Ba_2CdP_2$ . We calculated the electronic structure of  $Ba_2CdP_2$  with

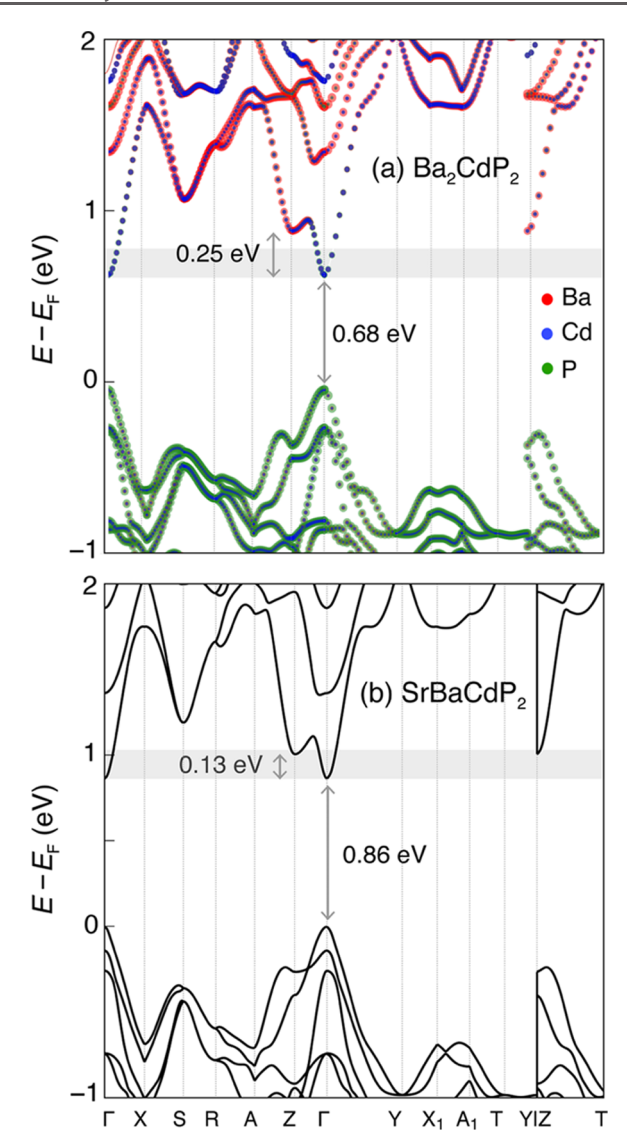
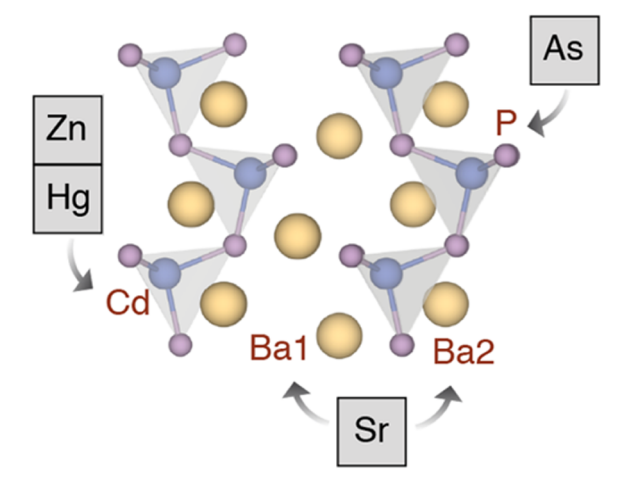


**Figure 4.** (a) Atom-decomposed electronic band structure of  $Ba_2CdP_2$  along the special k-point path of the Brillouin zone. In the conduction band, a higher-energy valley is located at Z, 0.25 eV above the conduction band minimum (CBM) at  $\Gamma$ . (b) In SrBaCdP<sub>2</sub>, the higher-energy valley at Z is 0.13 eV above the CBM.

relativistic spin—orbit coupling (SOC), the results of which are shown in Figure S4 of the Supporting Information. We find that the band gap, effective masses, and the energy separation between the two conduction band valleys remain unchanged. To systematically realize this conduction band convergence, we must first understand the atomic origin of the second conduction band valley.

The atom-decomposed electronic band structure (Figure 4a) reveals that the conduction band valley at Z is primarily composed of Ba-derived orbitals and a small fraction from Cd. Therefore, it may be possible to achieve band convergence by following the band engineering strategies outlined in Figure 1 and applying them on the Ba site. Figure 5 summarizes the two band engineering strategies that were computationally explored in this study. Although we only explored these strategies for Ba<sub>2</sub>CdP<sub>2</sub>, the same strategies can be extended to the other "2–1–2" phases, including Sr<sub>2</sub>CdP<sub>2</sub>. We first considered isovalent substitutions, which generate isostructural and ordered compounds with each Wyckoff site fully occupied by an

# (a) isovalent substitution



# (b) cation mutations

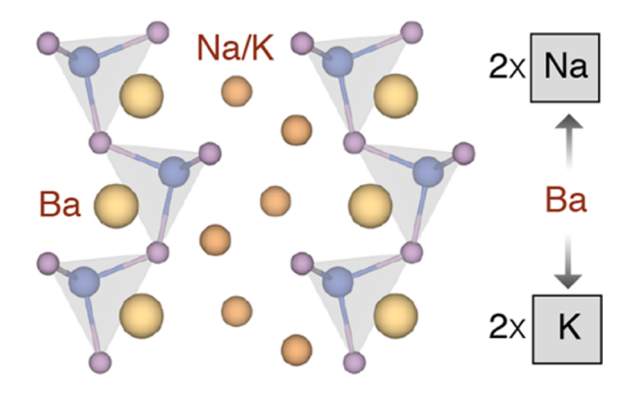


**Figure 5.** Band engineering strategies: (a) isovalent substitution and (b) cation mutations. For isovalent substitution, Ba is substituted with Sr, while Cd with Hg or Zn, and P with As. For cation mutations, each Ba atom is replaced with two alkali elements (Na, K), resulting in a hypothetical quaternary structure.

element, in contrast to disordered alloys where atomic sites are partially occupied.

For isovalent substitution (Figure 5a), we considered three different types of substitutions: (1) replacing Ba at sites 1 and 2 (Figure 2c/d), with Sr, (2) replacing Cd with either Zn or Hg, and (3) replacing P with As. For cation mutations, each divalent Ba cation is mutated into two alkali metal atoms, resulting in  $M_2BaCdP_2$  (M=Na,K) quaternary Zintl phases (Figure 5b). These quaternary Zintl phases (similar to the Sb-containing compounds discovered by our team in the past  $^{52}$ ) are also based upon  $[CdP_2]^{4-}$  polyanionic layers mentioned above, except that two alkali metal cations are occupying the interlayer space instead. To further explore ways to achieve band convergence, we also considered hybrid approaches, combining the two strategies, by applying isovalent substitutions on the alkali metal cation sites, mentioned above, creating hypothetical quinary phases MNBaCdP<sub>2</sub> (M, N=Na, K).

To check the effectiveness of each band engineering strategy, we calculated the electronic structure and determined the energy separation between the CBM and the second conduction band valley. The electronic structures for each of

these strategies are shown in Figure S1 in the Supporting Information.

For the isovalent substitution strategy, we found that the substitution of P with As leads to an increase in the energy separation between the first and second conduction band valleys (0.40 eV in Ba<sub>2</sub>CdAs<sub>2</sub>). Next, when Cd is substituted with Hg, the energy separation increases to 0.50 eV. However, the substitution of a Zn atom on the Cd site does facilitate band convergence with the energy separation reducing to 0.15 eV, provided Ba<sub>2</sub>ZnP<sub>2</sub> retains the original structure of Ba<sub>2</sub>CdP<sub>2</sub> (N.B. as already mentioned, Ba<sub>2</sub>ZnP<sub>2</sub> is reported to crystallize with a different structure; 56 however, bulk relaxation from DFT calculations supports the notion that Ba<sub>2</sub>ZnP<sub>2</sub> may also form in the Yb<sub>2</sub>CdSb<sub>2</sub> structure type). When substituting with Sr, there are two unique Wyckoff sites for Ba that could be replaced with Sr: site 1, located in between the layers, and site 2, interspersed within the tetrahedra (Figure 2). As a result, two hypothetical quaternary structures can be devised— SrBaCdP<sub>2</sub> (substitution on site 1) and BaSrCdP<sub>2</sub> (substitution on site 2). We found that SrBaCdP2 is energetically more favorable than BaSrCdP2. For SrBaCdP2, where Sr fully occupies site 1 and Ba fully occupies site 2, the energy separation between the first and second conduction band valleys is decreased to within 0.13 eV (Figure 4b). Consequently, the n-type thermoelectric performance of the hypothetical SrBaCdP<sub>2</sub> is 3-fold greater than that of Ba<sub>2</sub>CdP<sub>2</sub> (Table 3). The band effective mass  $m_b^*$  is lower than that of Ba<sub>2</sub>CdP<sub>2</sub> and Sr<sub>2</sub>CdP<sub>2</sub>, while the thermal conductivity is between the  $\kappa_L$  values of Ba<sub>2</sub>CdP<sub>2</sub> and Sr<sub>2</sub>CdP<sub>2</sub>. Notably, the electron mobility in SrBaCdP2 is predicted to be similar with Sr<sub>2</sub>CdP<sub>2</sub>, which is higher than Ba<sub>2</sub>CdP<sub>2</sub>.

**3.4.** Defect Chemistry of Ba<sub>2</sub>CdP<sub>2</sub> and SrBaCdP<sub>2</sub>. Although Ba<sub>2</sub>CdP<sub>2</sub> and SrBaCdP<sub>2</sub> are predicted to exhibit good n-type TE performance, the successful prediction relies on a key assumption: the material must be doped to the desired electron concentrations to maximize the TE potential. Therefore, we performed first-principles defect calculations to assess the n-type dopability for Ba<sub>2</sub>CdP<sub>2</sub> and SrBaCdP<sub>2</sub>.

3.4.1.  $Ba_2CdP_2$ . The formation energies  $(\Delta E_{D,q})$  of the native point defects in Ba<sub>2</sub>CdP<sub>2</sub> under Cd-rich growth conditions are shown in Figure 6a. We found that cation vacancies (V<sub>Cd</sub>, V<sub>Ba</sub>) are the primary acceptor defects in Ba<sub>2</sub>CdP<sub>2</sub>, with the Cd vacancies (V<sub>Cd</sub>) being the lowest-energy acceptors. This limits extrinsic n-type doping by charge compensating the doped electrons. The formation energy of V<sub>Cd</sub> is the highest (concentration is the lowest) under the most Cd-rich growth conditions, which corresponds to the most positive  $\Delta \mu_{Cd}$  within the phase stability region of Ba<sub>2</sub>CdP<sub>2</sub> (Figure 3a). Therefore, the defect energetics under the most Cd-rich condition is the best-case scenario for assessing the ntype dopability of Ba<sub>2</sub>CdP<sub>2</sub>. The most Cd-rich (and Ba-rich) growth condition is represented by the three-phase equilibrium between Cd-BaCd<sub>2</sub>-Ba<sub>2</sub>CdP<sub>2</sub> (yellow marker in Figure 3a inset). On the other hand, the p-type dopability is limited by low formation energies of donor defects V<sub>p</sub> and Cd<sub>p</sub>. Under Cd- and Ba-rich growth conditions (Figure 6a), the equilibrium Fermi energy (E<sub>F</sub>) lies above the mid-gap, indicating that Ba<sub>2</sub>CdP<sub>2</sub> is natively n-type. Interestingly, very few Zintl phases have been experimentally realized as n-type materials, making Ba2CdP2 a rarity among the class of Zintl phases. Also, the very high formation energy of  $V_{Cd}$  ( $\approx 0.7$  eV at the CBM) means that Ba2CdP2 could be effectively doped ntype with extrinsic dopants. The defect chemistry of Ba<sub>2</sub>CdP<sub>2</sub>

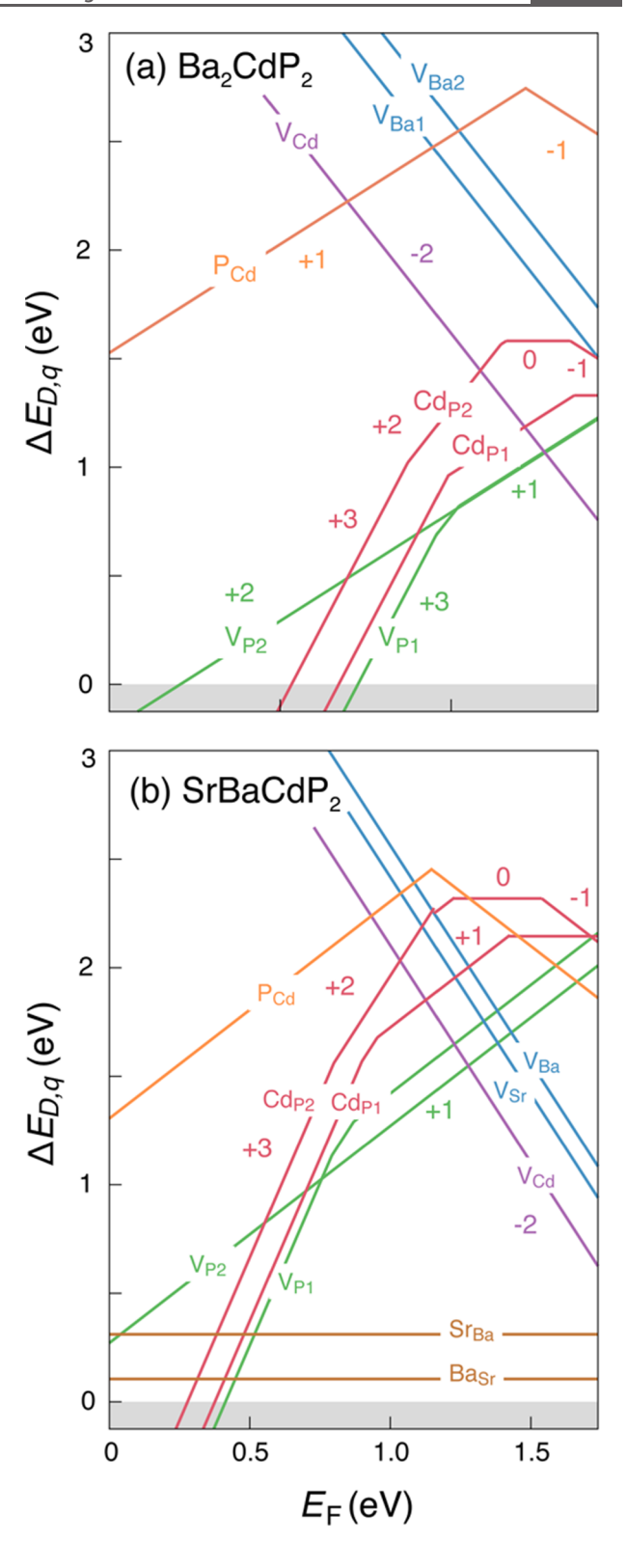


**Figure 6.** Formation energies of native point defects  $(\Delta E_{\mathrm{D},q})$  as a function of Fermi energy  $(E_{\mathrm{F}})$  for (a)  $\mathrm{Ba_2CdP_2}$  under the most Cd-and Ba-rich growth conditions and (b)  $\mathrm{SrBaCdP_2}$  under Cd-, Ba-, and Sr-rich growth conditions.  $E_{\mathrm{F}}$  is referenced to the valence band maximum. The DFT underestimation of the band gap is corrected by applying band edge shifts from GW calculations. The slope of a line is the charged state of the defect. The lowest-energy acceptor defect is Cd vacancy (in purple) in both  $\mathrm{Ba_2CdP_2}$  and  $\mathrm{SrBaCdP_2}$ .

breaks the common doping asymmetry of Zintl phases, where most Zintl phases are natively p-type and cannot be doped n-type. Therefore, Ba<sub>2</sub>CdP<sub>2</sub> is a promising and interesting candidate for TE applications.

3.4.2. SrBaCdP<sub>2</sub>. The defect chemistry of SrBaCdP<sub>2</sub> is generally similar to that of Ba2CdP2, with the predominant acceptor defects being  $V_{Cd}$ ,  $V_{Sr}$ , and  $V_{Ba}$ . The primary donor defects (V<sub>p</sub>, Cd<sub>p</sub>) are similar to those present in Ba<sub>2</sub>CdP<sub>2</sub>. Interestingly, the charge-neutral Sr/Ba antisite defects (Sr<sub>Ba</sub> and Ba<sub>Sr</sub>) have low formation energies, which indicates that SrBaCdP2 may exhibit some degree of site disorder at the Ba1 site. However, given that these antisite defects are charge neutral, they will not affect the overall dopability of SrBaCdP<sub>2</sub>, i.e., they will not cause charge (electron or hole) compensation. In an attempt to validate this computational prediction, a fast round of exploratory syntheses was performed. These very preliminary synthetic and structural studies showed assuring results, with the main product of one of the reactions identified as the quaternary phase with refined chemical composition  $Sr_{\approx 1.6}Ba_{\approx 0.4}CdP_2$  (or  $Sr_{1+x}Ba_{1-x}CdP_2$  with  $x \approx 0.6$ ). Although not fully ordered, Sr and Ba cations in the experimentally observed structure occupy the following positions—site 1 being an admixture of Sr and Ba (in approx. ratio 2:1), and site 2 taken by Sr. The outcome from this initial experiment is inline with the previous work on (Sr,Ba)2CdSb2,52 which is a testament to the difficulty in obtaining "1-1-1-2" material with fully ordered cations in the structure.

To assess the n-type dopability of SrBaCdP<sub>2</sub>, we again considered the most Cd-, Sr-, and Ba-rich growth conditions within the phase stability region (Table S3 in the Supporting Information). We found that the most Cd-, Sr-, and Ba-rich conditions are achieved at the four-phase corner, where SrBaCdP<sub>2</sub> is in equilibrium with BaCd<sub>2</sub>P<sub>2</sub>–Ba<sub>2</sub>CdP<sub>2</sub>–SrCd<sub>11</sub>. Under these conditions, the formation energies of  $V_{\rm Cd}$ ,  $V_{\rm Sr}$ , and  $V_{\rm Ba}$  are high; SrBaCdP<sub>2</sub> is natively n-type (equilibrium Fermi energy above the mid-gap), and it may be possible to introduce extrinsic donor dopants to further increase the free electron concentration. Further work is encouraged to explore extrinsic doping of Ba<sub>2</sub>CdP<sub>2</sub> and SrBaCdP<sub>2</sub> to optimize the TE performance.

# 4. CONCLUSIONS

In summary, we synthesized, structurally characterized, and interrogated the TE properties of the three isostructural Zintl phases A<sub>2</sub>CdP<sub>2</sub> (A = Sr, Ba, Eu), which crystallize in the Yb<sub>2</sub>CdSb<sub>2</sub> structure. Using first-principles calculations, we found that both Ba<sub>2</sub>CdP<sub>2</sub> and Sr<sub>2</sub>CdP<sub>2</sub> are thermodynamically stable and exhibit moderately high n-type TE performance. Following band convergence strategies, including isovalent substitution and cation mutations, we showed that band engineering *via* isovalent substitution of Sr on the Ba site, *i.e.*, SrBaCdP<sub>2</sub>, can improve the n-type TE performance of Ba<sub>2</sub>CdP<sub>2</sub> 3-fold by increasing the conduction band valley degeneracy. Furthermore, first-principles defect calculations show a large n-type dopability window for both Ba<sub>2</sub>CdP<sub>2</sub> and SrBaCdP<sub>2</sub>, which is a rarity among Zintl phases.

Additional studies into these and related isotypic compounds are highly encouraged to not only understand the origins of the doping asymmetry exhibited by Zintl phases but also expand the structural diversity among n-type dopable Zintl phases. Further tuning of the synthetic parameters could diminish the Sr and Ba disorder in Sr<sub>1+x</sub>Ba<sub>1-x</sub>CdP<sub>2</sub> and lead to the validation of the computational results with regard to

SrBaCdP<sub>2</sub> and its enhanced TE performance. Doping or alloying work not considered as a part of this paper can also create a material with excellent TE properties. Finally, future exploratory syntheses into the A-Cd-P (A=Ba, Sr, Eu) and M-A-Cd-P (M=Na, K) phase diagrams are anticipated to lead to new and interesting ternary and quaternary compounds with promising properties for thermoelectrics and/or photovoltaics.

# ASSOCIATED CONTENT

# Supporting Information

The Supporting Information is available free of charge at https://pubs.acs.org/doi/10.1021/acs.chemmater.0c03960.

Tables with atomic coordinates and equivalent displacement parameters for  $Sr_2CdP_2$  and  $Eu_2CdP_2$  and selected distances in  $Ba_2CdP_2$ ,  $Sr_2CdP_2$ , and  $Eu_2CdP_2$ ; fitted elemental-phase reference chemical potentials; figure showing the electronic structures of band engineering strategies for  $Ba_2CdP_2$  and phase stability of  $Sr_2CdP_2$ ; a table with data analysis of the phase stability region of  $SrBaCdP_2$  in quaternary Sr-Ba-Cd-P chemical potential space; figures showing the electronic structures of  $Sr_2CdP_2$ , and the electronic structures of  $Ba_2CdP_2$ , and  $SrBaCdP_2$  calculated with spin—orbit coupling (PDF)

# AUTHOR INFORMATION

# **Corresponding Authors**

Prashun Gorai — Colorado School of Mines, Golden, Colorado 80401, United States; orcid.org/0000-0001-7866-0672; Email: pgorai@mines.edu

Svilen Bobev — Department of Chemistry and Biochemistry, University of Delaware, Newark, Delaware 19716, United States; orcid.org/0000-0002-0780-4787; Email: bobev@udel.edu

### Authors

Adam Balvanz – Department of Chemistry and Biochemistry, University of Delaware, Newark, Delaware 19716, United States

Jiaxing Qu — Department of Mechanical Engineering, University of Illinois at Urbana—Champaign, Urbana, Illinois 61801, United States; orcid.org/0000-0002-3304-4996

Sviatoslav Baranets — Department of Chemistry and Biochemistry, University of Delaware, Newark, Delaware 19716, United States; Occid.org/0000-0003-3449-3344

Elif Ertekin — Department of Mechanical Engineering, University of Illinois at Urbana—Champaign, Urbana, Illinois 61801, United States; orcid.org/0000-0002-7816-1803

Complete contact information is available at: https://pubs.acs.org/10.1021/acs.chemmater.0c03960

# **Author Contributions**

 $\P$ A.B. and J.Q. contributed equally to this work. All authors have given approval to the final version of the manuscript.

### Notes

The authors declare no competing financial interest.

# ACKNOWLEDGMENTS

The experimental part of this research, conducted at the University of Delaware received financial support from the U.S. Department of Energy through a grant DE-SC0008885. A.B.

also acknowledges the University of Delaware's undergraduate research program. J.Q. was funded by the DIGI-MAT program from the NSF DGE program, grant no. 1922758. E.E. acknowledges support from the NSF DMR program, grant no. 1729149. The research was performed using computational resources sponsored by the Department of Energy's Office of Energy Efficiency and Renewable Energy located at the NREL.

#### REFERENCES

- (1) Nesper, R. Bonding Patterns in Intermetallic Compounds. *Angew. Chem., Int. Ed.* **1991**, 30, 789-817.
- (2) Nesper, R. The Zintl-Klemm Concept-A Historical Survey. Z. Anorg. Allg. Chem. 2014, 640, 2639–2648.
- (3) Zintl, E. Intermetallische Verbindungen. *Angew. Chem.* **1939**, *52*, 1–6.
- (4) Klemm, W. Einige Probleme Aus Der Physik Und Der Chemie Der Halbmetalle Und Der Metametalle. *Angew. Chem.* **1950**, *62*, 133–142.
- (5) Brown, S. R.; Kauzlarich, S. M.; Gascoin, F.; Snyder, G. J. Yb<sub>14</sub>MnSb<sub>11</sub>: New High Efficiency Thermoelectric Material for Power Generation. *Chem. Mater.* **2006**, *18*, 1873–1877.
- (6) Toberer, E. S.; Zevalkink, A.; Crisosto, N.; Snyder, G. J. The Zintl Compound Ca<sub>5</sub>Al<sub>2</sub>Sb<sub>6</sub> for Low-Cost Thermoelectric Power Generation. *Adv. Funct. Mater.* **2010**, *20*, 4375–4380.
- (7) Saramat, A.; Svensson, G.; Palmqvist, A. E. C.; Stiewe, C.; Mueller, E.; Platzek, D.; Williams, S. G. K.; Rowe, D. M.; Bryan, J. D.; Stucky, G. D. Large Thermoelectric Figure of Merit at High Temperature in Czochralski-Grown Clathrate Ba<sub>8</sub>Ga<sub>16</sub>Ge<sub>30</sub>. *J. Appl. Phys.* **2006**, *99*, No. 023708.
- (8) Slack, G. New Materials and Performance Limits for Thermoelectric Cooling. In *CRC Handbook of Thermoelectrics*; Rowe, D. M., Ed.; CRC Press: Boca Raton, FL, 1995; pp 407–441.
- (9) Schäfer, H. On the Problem of Polar Intermetallic Compounds: The Stimulation of E. Zintl's Work for the Modern Chemistry of Intermetallics. *Annu. Rev. Mater. Sci.* **1985**, *15*, 1–42.
- (10) Peng, W.; Chanakian, S.; Zevalkink, A. Crystal Chemistry and Thermoelectric Transport of Layered  $AM_2X_2$  Compounds. *Inorg. Chem. Front.* **2018**, *5*, 1744–1759.
- (11) Gorai, P.; Ganose, A.; Faghaninia, A.; Jain, A.; Stevanović, V. Computational Discovery of Promising New *n*-Type Dopable *ABX* Zintl Thermoelectric Materials. *Mater. Horiz.* **2020**, *7*, 1809–1818.
- (12) Chen, C.; Xue, W.; Li, S.; Zhang, Z.; Li, X.; Wang, X.; Liu, Y.; Sui, J.; Liu, X.; Cao, F.; Ren, Z.; Chu, C. W.; Wang, Y.; Zhang, Q. Zintl-Phase Eu<sub>2</sub>ZnSb<sub>2</sub>: A Promising Thermoelectric Material with Ultralow Thermal Conductivity. *Proc. Natl. Acad. Sci. U.S.A.* **2019**, *116*, 2831–2836.
- (13) Toberer, E. S.; May, A. F.; Melot, B. C.; Flage-Larsen, E.; Snyder, G. J. Electronic Structure and Transport in Thermoelectric Compounds  $AZn_2Sb_2$  (A = Sr, Ca, Yb, Eu). Dalton Trans. **2010**, 39, 1046–1054.
- (14) Zhang, H.; Baitinger, M.; Tang, M. B.; Man, Z. Y.; Chen, H. H.; Yang, X. X.; Liu, Y.; Chen, L.; Grin, Y.; Zhao, J. T. Thermoelectric Properties of  $Eu(Zn_{1-x}Cd_x)_2Sb_2$ . Dalton Trans. **2010**, 39, 1101–1104.
- (15) Cooley, J. A.; Promkhan, P.; Gangopadhyay, S.; Donadio, D.; Pickett, W. E.; Ortiz, B. R.; Toberer, E. S.; Kauzlarich, S. M. High Seebeck Coefficient and Unusually Low Thermal Conductivity Near Ambient Temperatures in Layered Compound Yb<sub>2-x</sub>Eu<sub>x</sub>CdSb<sub>2</sub>. *Chem. Mater.* **2018**, *30*, 484–493.
- (16) Xia, S.-Q.; Bobev, S. Cation-Anion Interactions as Structure Direction Factors: Structure and Bonding of Ca<sub>2</sub>CdSb<sub>2</sub> and Yb<sub>2</sub>CdSb<sub>2</sub>. *J. Am. Chem. Soc.* **2007**, *129*, 4049–4057.
- (17) Yan, J.; Gorai, P.; Ortiz, B.; Miller, S.; Barnett, S. A.; Mason, T.; Stevanović, V.; Toberer, E. S. Material Descriptors for Predicting Thermoelectric Performance. *Energy Environ. Sci.* **2015**, *8*, 983–994.
- (18) Heremans, J. P.; Jovovic, V.; Toberer, E. S.; Saramat, A.; Kurosaki, K.; Charoenphakdee, A.; Yamanaka, S.; Snyder, G. J. Enhancement of Thermoelectric Efficiency in PbTe by Distortion of the Electronic Density of States. *Science* **2008**, 321, 554–557.

- (19) Wang, S.; Tan, X.; Tan, G.; She, X.; Liu, W.; Li, H.; Liu, H.; Tang, X. The Realization of a High Thermoelectric Figure of Merit in Ge-Substituted  $\beta$ -Zn<sub>4</sub>Sb<sub>3</sub> through Band Structure Modification. *J. Mater. Chem.* **2012**, 22, 13977–13985.
- (20) Pei, Y.; Shi, X.; Lalonde, A.; Wang, H.; Chen, L.; Snyder, G. J. Convergence of Electronic Bands for High Performance Bulk Thermoelectrics. *Nature* **2011**, 473, 66–69.
- (21) Liu, W.; Tan, X.; Yin, K.; Liu, H.; Tang, X.; Shi, J.; Zhang, Q.; Uher, C. Convergence of Conduction Bands as a Means of Enhancing Thermoelectric Performance of *n*-Type Mg<sub>2</sub>Si<sub>1-x</sub>Sn<sub>x</sub> Solid Solutions. *Phys. Rev. Lett.* **2012**, *108*, No. 166601.
- (22) Tan, G.; Shi, F.; Hao, S.; Zhao, L. D.; Chi, H.; Zhang, X.; Uher, C.; Wolverton, C.; Dravid, V. P.; Kanatzidis, M. G. Non-Equilibrium Processing Leads to Record High Thermoelectric Figure of Merit in PbTe-SrTe. *Nat. Commun.* **2016**, *7*, No. 12167.
- (23) Zhao, L. D.; Wu, H. J.; Hao, S. Q.; Wu, C. I.; Zhou, X. Y.; Biswas, K.; He, J. Q.; Hogan, T. P.; Uher, C.; Wolverton, C.; Dravid, V. P.; Kanatzidis, M. G. All-Scale Hierarchical Thermoelectrics: MgTe in PbTe Facilitates Valence Band Convergence and Suppresses Bipolar Thermal Transport for High Performance. *Energy Environ. Sci.* 2013, 6, 3346–3355.
- (24) Imasato, K.; Kang, S. D.; Ohno, S.; Snyder, G. J. Band Engineering in Mg<sub>3</sub>Sb<sub>2</sub> by Alloying with Mg<sub>3</sub>Bi<sub>2</sub> for Enhanced Thermoelectric Performance. *Mater. Horiz.* **2018**, *5*, 59–64.
- (25) Jood, P.; Male, J.; Anand, S.; Matsushita, Y.; Takagiwa, Y.; Kanatzidis, M. G.; Snyder, G. J.; Ohta, M. Na Doping in PbTe Solubility, Band Convergence, Phase Boundary Mapping, and Thermoelectric Properties. *J. Am. Chem. Soc.* **2020**, *142*, 15464–15475.
- (26) Balvanz, A.; Baranets, S.; Bobev, S. Synthesis and Structural Characterization of the New Zintl Phases Ba<sub>3</sub>Cd<sub>2</sub>P<sub>4</sub> and Ba<sub>2</sub>Cd<sub>2</sub>P<sub>3</sub>. Rare Example of Small Gap Semiconducting Behavior with Negative Thermopower within the Range 300 K–700 K. *J. Solid State Chem.* **2020**, 289, No. 121476.
- (27) Baranets, S.; Bobev, S. From the Ternary Phase  $Ca_{14}Zn_{1+\delta}Sb_{11}$  ( $\delta\approx0.4$ ) to the Quaternary Solid Solutions  $Ca_{14-x}RE_xZnSb_{11}$  (RE=La-Nd, Sm, Gd,  $x\approx0.9$ ). A Tale of Electron Doping via Rare-Earth Metal Substitutions and the Concomitant Structural Transformations. *Inorg. Chem.* **2019**, *58*, 8506–8516.
- (28) Baranets, S.; Voss, L.; Stoyko, S.; Bobev, S. Synthesis, Crystal Structure and Physical Properties of the Solid Solutions  $Ca_{14-x}RE_xCdSb_{11}$  (RE=La-Nd, Sm, Gd-Yb,  $x\approx 0.85\pm 0.15$ ). *J. Appl. Phys.* **2019**, 125, No. 245101.
- (29) SAINT and SADABS; Bruker AXS Inc.: Madison, Wisconsin, 2014.
- (30) Sheldrick, G. M. SHELXT Integrated Space-Group and Crystal-Structure Determination. *Acta Crystallogr., Sect. A: Found. Adv.* **2015**, *71*, 3–8.
- (31) Dolomanov, O. V.; Bourhis, L. J.; Gildea, R. J.; Howard, J. A. K.; Puschmann, H. OLEX2: A Complete Structure Solution, Refinement and Analysis Program. *J. Appl. Crystallogr.* **2009**, 42, 339–341.
- (32) Sheldrick, G. M. Crystal Structure Refinement with SHELXL. Acta Crystallogr., Sect. C: Struct. Chem. 2015, 71, 3–8.
- (33) Kresse, G.; Furthmüller, J. Efficient Iterative Schemes for Ab Initio Total-Energy Calculations Using a Plane-Wave Basis Set. *Phys. Rev. B* **1996**, *54*, 11169–11186.
- (34) Blöchl, P. E. Projector Augmented-Wave Method. *Phys. Rev. B: Condens. Matter* **1994**, *50*, 17953–17979.
- (35) Perdew, J. P.; Burke, K.; Ernzerhof, M. Generalized Gradient Approximation Made Simple. *Phys. Rev. Lett.* **1996**, *77*, 3865–3868.
- (36) Setyawan, W.; Curtarolo, S. High-Throughput Electronic Band Structure Calculations: Challenges and Tools. *Comput. Mater. Sci.* **2010**, *49*, 299–312.
- (37) Miller, S. A.; Gorai, P.; Ortiz, B. R.; Goyal, A.; Gao, D.; Barnett, S. A.; Mason, T. O.; Snyder, G. J.; Lv, Q.; Stevanović, V.; Toberer, E. S. Capturing Anharmonicity in a Lattice Thermal Conductivity Model for High-Throughput Predictions. *Chem. Mater.* **2017**, *29*, 2494–2501.

- (38) Birch, F. Elasticity and Constitution of the Earth's Interior. *J. Geophys. Res.* **1952**, *57*, 227–286.
- (39) Rahim, W.; Skelton, J. M.; Scanlon, D. O. α-Bi<sub>2</sub>Sn<sub>2</sub>O<sub>7</sub>: a Potential Room Temperature n-Type Oxide Thermoelectric. *J. Mater. Chem. A* **2020**, *8*, 16405–16420.
- (40) Mizokami, K.; Togo, A.; Tanaka, I. Lattice Thermal Conductivities of Two SiO<sub>2</sub> Polymorphs by First-Principles Calculations and Phonon Boltzmann Transport Equation. *Phys. Rev. B: Condens. Matter* **2018**, 97, No. 224306.
- (41) Li, W.; Carrete, J.; Katcho, N. A.; Mingo, N. ShengBTE: A Solver of the Boltzmann Transport Equation for Phonons. *Comput. Phys. Commun.* **2014**, *185*, 1747–1758.
- (42) Puligheddu, M.; Xia, Y.; Chan, M.; Galli, G. Computational Prediction of Lattice Thermal Conductivity: A Comparison of Molecular Dynamics and Boltzmann Transport Approaches. *Phys. Rev. Mater.* **2019**, *3*, No. 085401.
- (43) Poncé, S.; Margine, E. R.; Verdi, C.; Giustino, F. EPW: Electron-Phonon Coupling, Transport and Superconducting Properties Using Maximally Localized Wannier Functions. *Comput. Phys. Commun.* **2016**, 209, 116–133.
- (44) Ganose, A. M.; Park, J.; Faghaninia, A.; Woods-Robinson, R.; Persson, K. A.; Jain, A. Efficient Calculation of Carrier Scattering Rates from First Principles. 2020, arXiv:2008.09734. arXiv.org e-Print archive. https://arxiv.org/abs/2008.09734 (accessed Nov 20, 2020).
- (45) Zhou, J. J.; Park, J.; Lu, I. T.; Maliyov, I.; Tong, X.; Bernardi, M. Perturbo: A Software Package for *Ab Inito* Electron-Phonon Interactions, Charge Transport and Ultrafast Dynamics. 2020, arXiv:2002.02045. arXiv.org e-Print archive. https://arxiv.org/abs/2002.02045 (accessed Nov 20, 2020).
- (46) Belkly, A.; Helderman, M.; Karen, V. L.; Ulkch, P. New Developments in the Inorganic Crystal Structure Database (ICSD): Accessibility in Support of Materials Research and Design. *Acta Crystallogr., Sect. B: Struct. Sci.* **2002**, *B58*, 364–369.
- (47) Stevanović, V.; Lany, S.; Zhang, X.; Zunger, A. Correcting Density Functional Theory for Accurate Predictions of Compound Enthalpies of Formation: Fitted Elemental-Phase Reference Energies. *Phys. Rev. B: Condens. Matter* **2012**, *85*, No. 115104.
- (48) Lany, S.; Zunger, A. Assessment of Correction Methods for the Band-Gap Problem and for Finite-Size Effects in Supercell Defect Calculations: Case Studies for ZnO and GaAs. *Phys. Rev. B: Condens. Matter* **2008**, 78, No. 235104.
- (49) Peng, H.; Scanlon, D. O.; Stevanović, V.; Vidal, J.; Watson, G. W.; Lany, S. Convergence of Density and Hybrid Functional Defect Calculations for Compound Semiconductors. *Phys. Rev. B: Condens. Matter* **2013**, 88, No. 115201.
- (50) Goyal, A.; Gorai, P.; Peng, H.; Lany, S.; Stevanović, V. A Computational Framework for Automation of Point Defect Calculations. *Comput. Mater. Sci.* **2017**, *130*, 1–9.
- (51) Wang, J.; Yang, M.; Pan, M. Y.; Xia, S.-Q.; Tao, X.-T.; He, H.; Darone, G.; Bobev, S. Synthesis, Crystal and Electronic Structures, and Properties of the New Pnictide Semiconductors  $A_2$ Cd $Pn_2$  (A = Ca, Sr, Ba, Eu; Pn = P, As). Inorg. Chem. **2011**, 50, 8020–8027.
- (52) Saparov, B.; Saito, M.; Bobev, S. Syntheses, and Crystal and Electronic Structures of the New Zintl Phases  $Na_2ACdSb_2$  and  $K_2ACdSb_2$  (A = Ca, Sr, Ba, Eu, Yb): Structural Relationship with  $Yb_2CdSb_2$  and the Solid solutions  $Sr_{2-x}A_xCdSb_2$ ,  $Ba_{2-x}A_xCdSb_2$  and  $Eu_{2-x}Yb_xCdSb_2$ . J. Solid State Chem. **2011**, 184, 432–440.
- (53) Shannon, R. D. Revised Effective Ionic Radii and Systematic Studies of Interatomic Distances in Halides and Chalcogenides. *Acta Crystallogr. A* **1976**, 32, 751–767. These effective ionic radii are not for coordination number CN 5, which is the case in the structures under consideration. Nonetheless, the discussed values provide a general trend, which is expected to be followed
- (54) Baranets, S.; Darone, G. M.; Bobev, S. Synthesis and Structure of  $Sr_{14}Zn_{1+x}As_{11}$  and  $Eu_{14}Zn_{1+x}As_{11}$  ( $x \le 0.5$ ). New Members of the Family of Pnictides Isotypic with  $Ca_{14}AlSb_{11}$ , Exhibiting a New Type of Structural Disorder. *J. Solid State Chem.* **2019**, 280, No. 120990.

- (55) Rajput, K.; Baranets, S.; Bobev, S. Observation of an Unexpected *n*-Type Semiconducting Behavior in the New Ternary Zintl Phase Eu<sub>3</sub>InAs<sub>3</sub>. *Chem. Mater.* **2020**, *32*, 9616–9626.
- (56) Balvanz, A.; Baranets, S.; Bobev, S. Synthesis, Structural Characterization, and Electronic Structure of the Novel Zintl Phase Ba<sub>2</sub>ZnP<sub>2</sub>. Acta Crystallogr., Sect. C: Struct. Chem. **2020**, 76, 869–873.
- (57) Saparov, B.; Broda, M.; Ramanujachary, K. V.; Bobev, S. New Quarternary Zintl Phases—Synthesis, Crystal and Electronic Strucutres of  $KA_2Cd_2Sb_3$  (A = Ca, Sr, Ba, Eu, Yb). Polyhedron **2010**, 29, 456–462.
- (58) Ohno, S.; Imasato, K.; Anand, S.; Tamaki, H.; Kang, S. D.; Gorai, P.; Sato, H. K.; Toberer, E. S.; Kanno, T.; Snyder, G. J. Phase Boundary Mapping to Obtain n-Type Mg<sub>3</sub>Sb<sub>2</sub>-Based Thermoelectrics. *Joule* **2018**, *2*, 141–154.